16. B. A. Jacobs *et al.*, *J. Am. Chem. Soc.* **113**, 4390 (1991).
17. I.-J. Chang, J. R. Winkler, H. B. Gray, *ibid.*, p. 7056.
18. M. J. Therien, M. A. Selman, H. B. Gray, I.-J. Chang, J. R. Winkler, *ibid.* **112**, 2420 (1990).
19. B. E. Bowler, T. J. Meade, S. L. Mayo, J. H. Richards, H. B. Gray, *ibid.* **111**, 8757 (1989).
20. D. S. Wuttke, J. R. Winkler, H. B. Gray, in preparation.
21. The coordinates of the 1.94 Å structure of horse heart cytochrome c (His$^{33}$ and His$^{72}$ calculations) [G. W. Bushnell, G. V. Louie, G. D. Brayer, *J. Mol. Biol.* **214**, 585 (1990)] and the 1.23 Å structure of yeast-iso-1 cytochrome c (His$^{39}$ and His$^{62}$ calculations) [G. V. Louie and G. D. Brayer, *J. Mol. Biol.* **214**, 527 (1990)] were provided by G. D. Brayer. Energy minimization (*19*) of each structure with Ru(bpy)$_2$(im) attached to His$^X$ did not significantly change any edge-edge distance.
22. We measured rates of $Fe^{2+} \rightarrow Ru^{3+}$ ET using a flash-quench technique (*17*). We prepared metastable Ru(bpy)$_2$(im)(His$^X$)$^{3+}$-Fe$^{2+}$-cyt c in less than 100 ns by quenching a small fraction of *Ru(bpy)$_2$(im)(His$^X$)$^{2+}$-Fe$^{2+}$-cyt c with Ru(NH$_3$)$_6^{3+}$. Intramolecular $Fe^{2+} \rightarrow Ru^{3+}$ ET was readily observed at 550 and 400 nm ($Fe^{2+}/Fe^{3+}$) and 504 and 306 nm ($Ru^{3+}/Ru^{2+}$) after 480-nm excitation (~25-ns pulse width). Rates of intramolecular $*Ru^{2+} \rightarrow Fe^{3+}$ ET could not be determined directly from the $*Ru^{2+}$ decay kinetics because the rates are substantially slower than the intrinsic excited-state decay ($k_d = 1.4 \times 10^7\ s^{-1}$). Instead, $*Ru^{2+} \rightarrow Fe^{3+}$ ET rates were extracted from the yield of Ru(bpy)$_2$(im)(His$^X$)$^{3+}$-Fe$^{2+}$-cyt c [formed from *Ru(bpy)$_2$(im)(His$^X$)$^{3+}$-Fe$^{3+}$-cyt c].
23. According to semiclassical ET theory, rates become activationless when the reaction driving force ($-\Delta G°$) equals the reorganization energy ($\lambda$) (*1*). This reorganization energy has been estimated to be 0.8 eV for Ru(bpy)$_2$(im)(His)-cyt c reactions (*17*). The activationless (maximum) rates are limited by an electronic factor,
$$k_{max} = (4\pi^3/h^2\ \lambda k_b T)^{1/2} H_{AB}^2$$
where $k_b$ is Boltzmann's constant, $T$ is temperature, $h$ is Planck's constant, and $H_{AB}$ is the matrix element that couples the reactants and products at the transition state.
24. B. E. Bowler, A. L. Raphael, H. B. Gray, *Prog. Inorg. Chem.* **38**, 259 (1990).
25. Activationless intraprotein ET spanning twelve orders of magnitude in rate and nearly 19 Å in redox-site separation has been interpreted in terms of edge-edge exponential decay with 1.4 Å$^{-1}$ slope and $1 \times 10^{13}\ s^{-1}$ intercept [C. C. Moser, J. M. Keske, K. Warncke, R. S. Farid, P. L. Dutton, *Nature* **355**, 796 (1992)]. Implicit in this interpretation is the assumption that the intervening polypeptide can be treated as a homogeneous medium. This correlation, then, serves as a reference line; deviations from this line indicate situations in which inhomogeneities of the intervening peptide must be considered. Because one (X = 72) of our $k_{max}$ values falls four orders of magnitude below this edge-edge exponential-decay line, and two others (X = 33, 62) deviate from the line by more than a factor of 50, analysis in terms of the structure of the intervening medium is called for. In this context, it is of interest that calculations based on an inhomogeneous aperiodic lattice model give electronic couplings (X = 33, 39, 62) in good agreement with our experimentally derived values (*9*).
26. Another (nearly equivalent) pathway exists for His$^{62}$ (*19*). The pathway consists of 12 covalent bonds and a space jump of 3.6 Å. The $\sigma$-tunneling length is 30.5 Å.
27. G. L. Closs and J. R. Miller, *Science* **240**, 440 (1988).
28. The electron donor in the *Ru(bpy)$_2$(im)(His$^X$)$^{2+}$ charge-transfer excited state is a bpy radical anion (*17*). The estimated order of $H_{AB}$ values (62 ~ 33 ~ 72 < 39) for the bpy anion $\rightarrow Fe^{3+}$ ET reactions differs from that derived from the $Fe^{2+} \rightarrow Ru^{3+}$ rates. No interpretation of these couplings is offered; among the many uncertainties are the nature and magnitude of donor (bpy anion) couplings to groups on the protein surface.
29. We thank D. N. Beratan for assistance with the pathway analyses and for many helpful discussions. D.S.W. acknowledges an NSF predoctoral fellowship and a fellowship from the Parsons Foundation. M.J.B. was the Carlsberg Foundation Scholar in the Beckman Institute during 1990–91. Supported by National Science Foundation grants CHE-8822988 and CHE-9119992.

27 December 1991; accepted 10 March 1992

# High-Resolution Imaging by Fourier Transform X-ray Holography

Ian McNulty,* Janos Kirz, Chris Jacobsen, Erik H. Anderson, Malcolm R. Howells,† Dieter P. Kern

**Fourier transform x-ray holography has been used to image gold test objects with submicrometer structure, resolving features as small as 60 nanometers. The hologram-recording instrument uses coherent 3.4-nanometer radiation from the soft x-ray undulator beamline X1A at the National Synchrotron Light Source. The specimen to be imaged is placed near the first-order focal spot produced by a Fresnel zone plate; the other orders, chiefly the zeroth, illuminate the specimen. The wave scattered by the specimen interferes with the spherical reference wave from the focal spot, forming a hologram with fringes of low spatial frequency. The hologram is recorded in digital form by a charge-coupled device camera, and the specimen image is obtained by numerical reconstruction.**

Soft x-ray microscopy offers the means to image thick, wet, unstained biological objects at high resolution with less damage than by electron probes (*1*, *2*). X-ray holographic microscopy offers good transverse and limited depth resolution from single exposures, is able to form both amplitude and phase-contrast images, and is amenable to flash exposure with pulsed sources. Fourier transform holography is especially suited to high-resolution x-ray imaging with digital recording and to rapid (minutes or less) numerical reconstruction of the holograms. We present experimental evidence that Fourier transform x-ray holography can operate near the resolution limit set by the optical design, which, in our case, is 60 nm.

Baez (*3*), Stroke (*4*), and Winthrop and Worthington (*5*) developed the conceptual foundations for x-ray holography and were among the first to advocate high-resolution holographic microscopy at x-ray wavelengths. Soon afterward, Rogers and Palmer (*6*) proposed the use of zone plates as beam splitters for x-ray holography. Following these and related theoretical developments, Aoki *et al.* (*7*) and Reuter and Mahr (*8*) performed pioneering demonstration experiments; they achieved modest resolution in spite of the severe limitations in coherent power then available. Subsequently, Kondratenko and Skrinsky (*9*) and Howells and Kirz (*10*) suggested that radiation from undulators in electron storage rings provides the required coherent flux for submicrometer holography and advocated the Fourier transform geometry with electronic detectors. Solem and co-workers (*11–13*) examined the possibilities of flash "snapshot" holography with x-ray lasers. They established requirements for coherence, power, and pulse length for successful imaging before the specimen is altered by motion, radiation damage, or thermal explosion. The flash approach potentially circumvents the damage issue and, in the case of the Fourier transform method, may result in lower average power levels on the detector. Haddad *et al.* (*14*) proposed flash x-ray holography with reflective reference scatterers, combined with charge-coupled device (CCD) detection.

Recently, undulator radiation has been used to demonstrate high-resolution Gabor x-ray holography (*15*) both at the National Synchrotron Light Source (NSLS) (*16*) and at Laboratoire d'Utilisation du Rayonnement Electromagnétique (LURE) (*17*). Biological specimens have been imaged with this technique at 56-nm resolution, and there are indications that the holograms contain information recorded near the ~20-nm resolution limit imposed by the photoresist detectors used (*16*). Using an x-ray laser to make 200-ps flash exposures, Trebes *et al.* (*18*) recorded Gabor holograms with 5-μm resolution. The attainable resolution with Gabor holography is ultimately limited to the detector resolution

I. McNulty, J. Kirz, C. Jacobsen, Physics Department, State University of New York, Stony Brook, NY 11794–3800.
E. H. Anderson and M. R. Howells, Lawrence Berkeley Laboratory, Berkeley, CA 94720.
D. P. Kern, IBM Thomas J. Watson Research Center, Yorktown Heights, NY 10598.

*To whom correspondence should be addressed at Advanced Photon Source, Argonne National Laboratory, 9700 South Cass Avenue, Argonne, IL 60439.
†Currently on leave at European Synchrotron Radiation Facility, BP220, 38043 Grenoble, France.

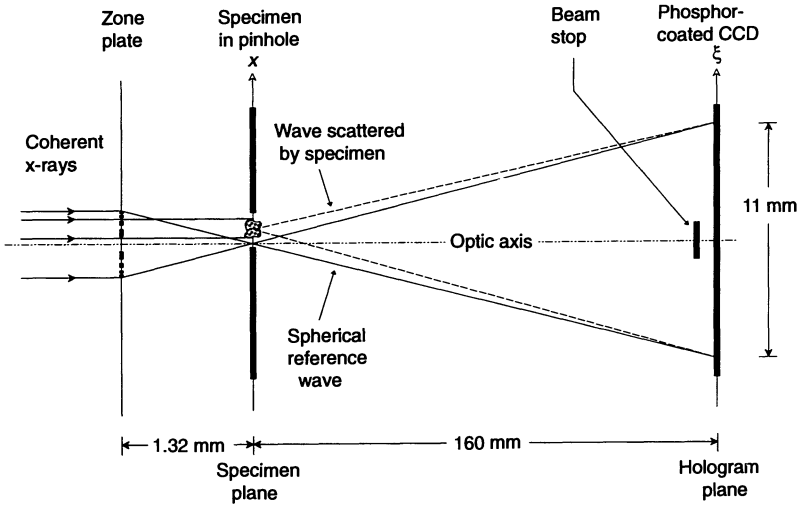


**Fig. 1.** Schematic diagram of the apparatus. A coherent x-ray beam illuminates the zone plate (shown in profile). The undeviated wave illuminates the specimen, and the focused wave serves as the reference source. A CCD detector records the interference between the specimen and reference waves. The x-rays not scattered by the specimen are blocked by the beam stop to prevent saturation of the CCD.

and readout method. In addition, although large image fields can be accommodated with partially coherent sources, the object field must be reasonably sparse in order not to corrupt the reference beam.

In Fourier transform holography, the imaging resolution is limited by the size of the reference source, the precision with which the reference wave front is known, and the angular extent over which the hologram can be recorded. In principle, the resolution of holograms recorded with extended reference sources can be improved by extended-source compensation (*19*). The detector resolution in this geometry sets the limit on the size of the object field that can be imaged. We used a Fresnel zone plate to form the reference wave, a CCD array to detect the holograms, and a digital computer to reconstruct them (*20, 21*).

The X1A undulator beamline at the NSLS supplies the apparatus (Fig. 1) with coherent soft x-radiation; the source and beamline have been described (*22*). A silicon nitride exit window (*23*) terminates the beamline vacuum system. The required temporal coherence is provided by a spherical grating monochromator. Spatial coherence over much of the zone plate area is provided by the small vertical source size at the undulator and by the small horizontal width of the monochromator exit slit. In a typical operating configuration the resolving power of the monochromator is 200, corresponding to a longitudinal coherence length of $\lambda^2/\Delta\lambda \approx 0.7$ μm. At the zone plate, the transverse coherence width of the beam is at least 50 μm. The coherent flux incident on the zone plate is $5 \times 10^7$ photons $s^{-1}$ for an electron beam current of 150 mA in the storage ring.

The zone plate, from which we derive both the reference wave and the object illumination, is mounted in a helium-filled enclosure just downstream of the beamline window. It was fabricated by electron beam lithography under a Center for X-ray Optics–IBM collaborative agreement (*24*). It has 450 zones, its diameter is 90 μm, and the focal length is 1.3 mm at a wavelength of 3.4 nm. Alternate zones are made of 60-nm-thick gold, and the finest zone is 50 nm wide. In the plane of the first-order focus, where the specimen is mounted, the focused flux is $2 \times 10^6$ photons $s^{-1}$, whereas the flux incident on the specimen (principally the unfocused, zeroth-order beam) is $4 \times 10^3$ photons $\mu m^{-2}$ $s^{-1}$. The focus is a slightly modified Airy pattern with 60-nm radius, as verified by scanning a sharp edge in the focal plane. The angular extent of the hologram, 90 μm/1.3 mm = 69 mrad, is determined by the numerical aperture of the zone plate.

Specimens are aligned in the focal plane on a precision *xyz* manipulator. For test objects we used fine gold patterns (Fig. 2, A and B) fabricated in the same manner as the zone plates. The patterns are surrounded by opaque frames. The focal spot is positioned near the corner of the frame such that the reference source is situated about 7 μm from the structure to be imaged. The alignment is verified by examining the transmitted flux distribution with a small pinhole scanned in front of a proportional counter. Ideally, this scanned image shows the fully illuminated specimen in projection as well as the unobscured reference wave diverging to a uniform disk. In practice, the uniformity of the disk may not be ideal because of imperfections in the zone plate and partial blockage of the reference wave by the specimen. To record the specimen's hologram, we retract the pinhole and proportional counter and insert a CCD camera with its entrance window in close proximity (≲0.5 mm) to the specimen.

A light-tight vacuum enclosure houses the CCD camera. The x-rays are admitted into it through an aluminized silicon nitride window. The CCD detector itself has 23-μm-square pixels and an active area of 9 by 13 mm (*25*). It is set back 16 cm from the camera window. To sensitize the CCD to x-rays, a thin (~10 μm) layer of P31 phosphor particles was deposited by sedimentation in a filtered methanol bath on the bare semiconductor surface. The P31 phosphor emits a green photon for roughly every 8 eV deposited (*26*), yielding >40 photons for each 3.4-nm x-ray. We estimate that 20% of these contribute to detectable charge in the CCD. The phosphor screen also protects the CCD from radiation damage, as it absorbs most of the x-rays. The CCD is cooled by thermal contact with a liquid nitrogen reservoir to reduce the dark current. After an exposure, data from the CCD are read into computer memory through a 16-bit analog-to-digital converter. Hologram exposures typically last 10 to 30 min.

Most of the x-rays incident on the specimen are not diffracted by it but are either absorbed in the specimen or transmitted to form an intense spot at the center of the hologram. To prevent saturation and nonlinearities resulting from overexposure of the detector, a small beam stop is suspended in front of the CCD chip and aligned with the on-axis beam.

Stability is of considerable importance in view of the relatively long exposures required to obtain good holograms. The most sensitive parameter is the position of the specimen in relation to the reference source, the zone plate focus. This alignment must be maintained to a precision at least as good as the desired resolution. To minimize drift and vibration, the specimen stage is mounted directly from the zone plate support, the environment temperature is controlled to within ±1°C, and the entire instrument is mounted on a granite bench with damped pneumatic legs.

Soft x-ray holograms of the test objects (Fig. 2, A and B) are shown in Fig. 2, C and D. The footprint of the reference beam appears as the overall circular outline, with the edges of the CCD detector cutting the two sides. The diameter of the pattern is 11 mm, except where an edge in the test object has obscured part of the reference wave (bottom portion of Fig. 2D). The shadow of the beam stop is visible at the center of the holograms. Two different beam stops are used, a vertical wire (Fig.

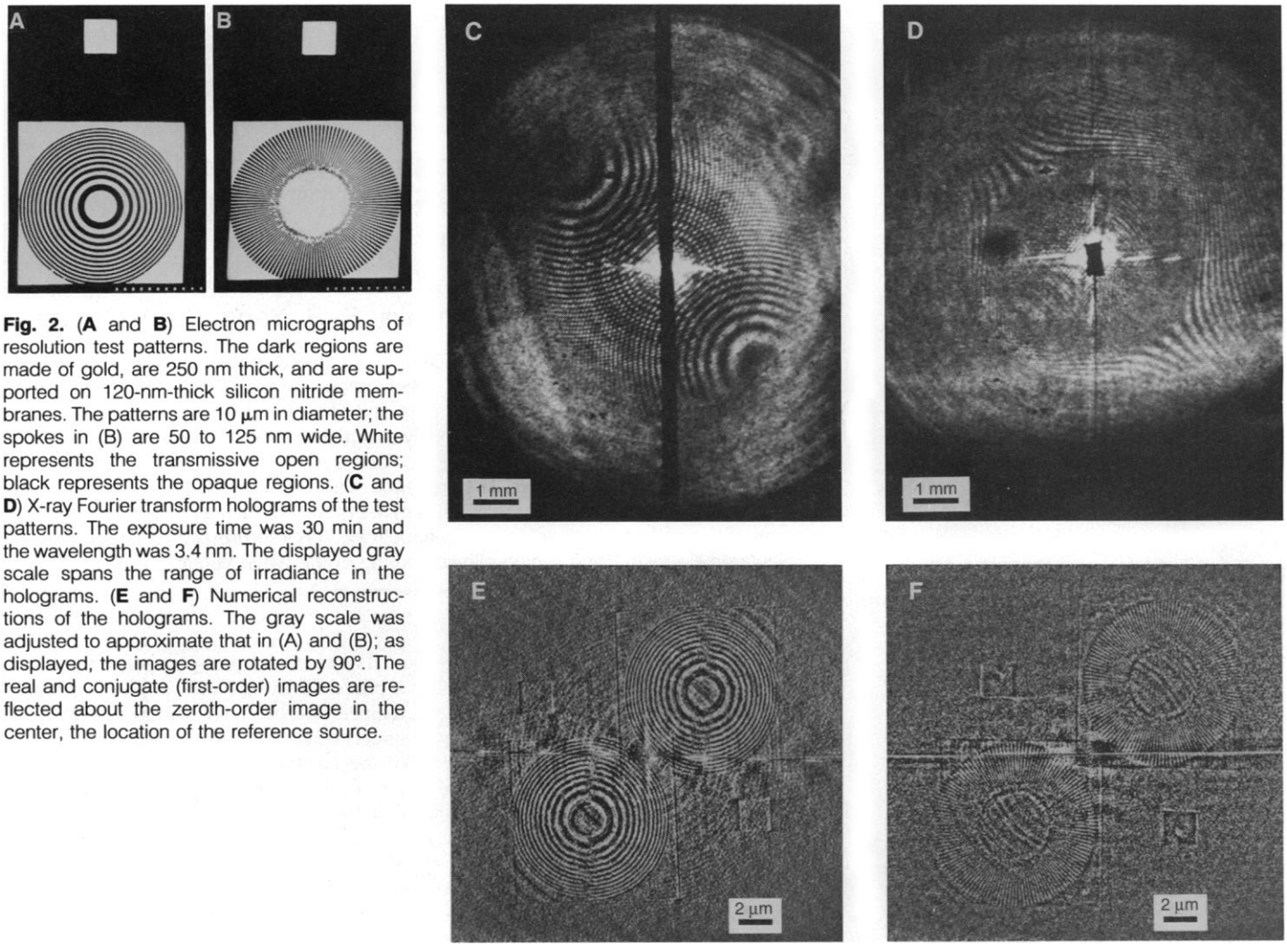


**Fig. 2.** (**A** and **B**) Electron micrographs of resolution test patterns. The dark regions are made of gold, are 250 nm thick, and are supported on 120-nm-thick silicon nitride membranes. The patterns are 10 μm in diameter; the spokes in (B) are 50 to 125 nm wide. White represents the transmissive open regions; black represents the opaque regions. (**C** and **D**) X-ray Fourier transform holograms of the test patterns. The exposure time was 30 min and the wavelength was 3.4 nm. The displayed gray scale spans the range of irradiance in the holograms. (**E** and **F**) Numerical reconstructions of the holograms. The gray scale was adjusted to approximate that in (A) and (B); as displayed, the images are rotated by 90°. The real and conjugate (first-order) images are reflected about the zeroth-order image in the center, the location of the reference source.

2C) and a rectangular plate suspended from a thread (Fig. 2D). Fringes due to the interference between the object and reference waves are visible nearly to the edge of the pattern, indicating the presence of information encoded up to the highest spatial frequencies permitted by the zone plate, namely 8.2 $\mu m^{-1}$, according to the Rayleigh criterion.

The hologram data were recorded and processed with a DEC VAXstation computer. To diminish their influence on the object reconstruction, we set CCD pixels exceeding a fixed saturation threshold to the mean signal levels of their neighbors. The average signal offset contributed by the camera and the dc background signal were subtracted. Thus corrected, the holograms were reconstructed with a discrete fast Fourier transform approximation to the continuous two-dimensional Fourier transformation,

$$A(x,y) = \iint I(\xi,\eta) \times \exp\left[-\frac{2\pi i}{\lambda z}(\xi x + \eta y)\right] d\xi d\eta \quad (1)$$

where $A(x,y)$ is proportional to the reconstruction amplitude, $I(\xi,\eta)$ is the hologram irradiance, $\lambda$ is the wavelength, $(x,y)$ and $(\xi,\eta)$ are space coordinates in the object and hologram planes, respectively, $z$ is the distance from the object plane to the detector, and $i = \sqrt{-1}$. The numerical procedure is similar to one we developed to model hologram formation (*21*). Each hologram required about 2 min of computation to reconstruct.

The results are shown in Fig. 2, E and F. As expected, the specimen image and its conjugate are seen in an antisymmetric arrangement. The highest spatial frequencies of the test pattern are well reproduced. The lower spatial frequencies, corresponding to the larger scale features of the test patterns, are somewhat degraded because the beam stop blocked the central region of the hologram where the low frequencies are encoded.

The finest features imaged in these experiments were 60-nm lines and spaces, representing an improvement of well over an order of magnitude compared to earlier work (*27*). These results demonstrate that a resolution consistent with diffraction limits is obtainable with a suitably coherent x-ray beam supplied by a high-brightness undulator, a spherical reference wave formed by a high-resolution zone plate, and the convenient and linear detection that a CCD camera offers. Digital recording of the hologram enables rapid numerical reconstruction of the image. However, these experiments did not address three-dimensional imaging. As determined by the numerical aperture of the current system, the depth resolution is ~4 μm, and our specimens appear two dimensional on that scale. At this level of performance the technique is still of limited use. The ultimate objective is to develop flash holography of biological specimens with 10- to 20-nm resolution in all three dimensions (*11*, *28*), an achievement that would have dramatic implications for structural biology.

## REFERENCES AND NOTES

1. D. Sayre, J. Kirz, R. Feder, D. M. Kim, E. Spiller, *Science* **196**, 1339 (1977).
2. For example, see A. Michette, G. R. Morrison, C. Buckley, Eds., *X-Ray Microscopy III* (Springer-

Verlag, Berlin, 1992).
3. A. V. Baez, *J. Opt. Soc. Am.* **42**, 756 (1952).
4. G. W. Stroke, *Appl. Phys. Lett.* **6**, 201 (1965).
5. J. T. Winthrop and C. R. Worthington, *Phys. Lett.* **15**, 124 (1965); *ibid.* **21**, 413 (1966).
6. G. L. Rogers and J. Palmer, *J. Microsc. (Oxford)* **89**, 125 (1969).
7. S. Aoki and S. Kikuta, *Jpn. J. Appl. Phys.* **13**, 1385 (1974).
8. B. Reuter and H. Mahr, *J. Phys. E* **9**, 746 (1976).
9. A. M. Kondratenko and A. N. Skrinsky, *Opt. Spectrosc. (USSR)* **42**, 189 (1977), in *Optical Information Processing*, E. S. Barrekette, G. W. Stroke, Y. E. Nesterikhin, W. E. Kock, Eds. (Plenum, New York, 1978), vol. 2, p. 1.
10. M. Howells and J. Kirz, *AIP Conf. Proc.* **118**, 85 (1984).
11. J. C. Solem and G. C. Baldwin, *Science* **218**, 229 (1982).
12. J. C. Solem, *J. Opt. Soc. Am.* **B3**, 1551 (1986).
13. _____ and G. F. Chapline, *Opt. Eng.* **23**, 193 (1984).
14. W. S. Haddad, D. Cullen, J. C. Solem, K. Boyer, C. K. Rhodes, in *OSA Proceedings on Short Wavelength Coherent Radiation: Generation and Applications*, R. W. Falcone and J. Kirz, Eds. (Optical Society of America, Washington, DC, 1988), vol. 2, p. 284.
15. In Gabor x-ray holography, a plane wave serves both to illuminate the specimen and to provide a reference wave that is collinear with it. The interference pattern between the object wave and the in-line reference wave is recorded on a high-resolution detector such as the x-ray resist polymethylmethacrylate (PMMA). X-ray Gabor holograms can be reconstructed optically (*17*) or enlarged with electron or atomic force microscopy and reconstructed numerically (*16*).
16. M. Howells *et al.*, *Science* **238**, 514 (1987), C Jacobsen, M. Howells, J. Kirz, S. Rothman, *J. Opt. Soc. Am.* **A7**, 1847 (1990).
17. D. Joyeux, S. Lowenthal, F. Polack, A. Bernstein, in *X-Ray Microscopy II*, D. Sayre, M. Howells, J. Kirz, H. Rarback, Eds. (Springer-Verlag, Berlin, 1988), p. 246, D. Joyeux and F. Polack, in *OSA Proceedings on Short Wavelength Coherent Radiation: Generation and Applications*, R. W. Falcone and J. Kirz, Eds. (Optical Society of America, Washington, DC, 1988), vol. 2, p. 295.
18. J. E. Trebes *et al.*, *Science* **238**, 517 (1987).
19. G. W. Stroke, R. Restrick, A. Funkhouser, D. Brumm, *Phys. Lett.* **18**, 274 (1965).
20. I. McNulty *et al.*, *Nucl. Instrum Methods* **A291**, 74 (1990).
21. I. McNulty, thesis, State University of New York at Stony Brook (1991).
22. H. Rarback *et al.*, *J. X-ray Sci. Technol.* **2**, 274 (1990).
23. All windows, as well as the zone plate and specimen substrates, consist of 250-μm-square, 100- to 120-nm-thick silicon nitride membranes supported by silicon frames. These membranes transmit 61 to 66% of the incident radiation at 3.4 nm.
24. E. Anderson, *SPIE Proc.* **1160**, 2 (1990).
25. The CCD (model TH7883CDA-NF) was made by Thomson Composants Militaires et Spatiaux, Courbevoie, France. The optically sensitive portion of the array is a single field of 576 by 384 pixels.
26. The high-efficiency phosphor P31 (ZnS·Cu) is commonly used in cathode ray tube displays. See R. Hertel, *Reference Data for Radio Engineers* (ITT Electro-Optics Corp., Fort Wayne, IN, 1975), pp. 17–35. We are grateful to R. Peterson for the phosphor coating.
27. S. Aoki and S. Kikuta, in *AIP Conf. Proc.* **147**, 49 (1986).
28. J. Brase, T J. Yorkey, D C. Peters, in "X-ray microimaging for the life sciences," *Lawrence Berkeley Laboratory Report LBL-27660*, D. T. Attwood and B. Barton, Eds. (Lawrence Berkeley Laboratory, Berkeley, CA, 1989), p. 74.
29. Zone plate and test object fabrication were supported by D. Attwood under U.S. Department of Energy grant DE-AC03-76SF00098. F. Camillo, C.-H. Ko, E. Kohandoust, S. Lindaas, H Rarback, S. Rock, and X. Zhang provided valuable assistance. We thank D. Sayre for helpful comments and stimulating discussion. The work was supported by the U.S. Department of Energy under grant DE-FG02-89ER60858 and carried out at the NSLS, which is supported by the U.S. Department of Energy Office of Basic Energy Sciences.

2 December 1991; accepted 16 March 1992

# Order and Low Dimensionality in the Organic Superconductor $(BEDT\text{-}TTF)_2Cu(NCS)_2$ Revealed by STM

R. Fainchtein,* S. T. D'Arcangelis, S. S. Yang, D. O. Cowan

**Single-crystal samples of $[(BEDT\text{-}TTF)_2]^+[Cu(NCS)_2]^-$ were synthesized and studied with a scanning tunneling microscope (STM). Real-space images of the anion and cation surfaces with molecular resolution were obtained. The images show no evidence of structural disorder or stacking faults previously suggested. The presence of an additional modulation commensurate with the lattice provides evidence of a lattice distortion. The cause of this modulation is unknown. The presence of a charge density wave in the material would have implications on the dimensionality of the material that may explain the peculiar temperature dependence of the electrical conductivity. This interpretation is consistent with the calculated Fermi surface, which allows nesting of the wave vector.**

The recent progress in the race to increase the superconducting transition temperature ($T_c$) in organic materials has been motivated by the discovery of the superconducting properties of the κ-phase (BEDT-TTF) (or ET) compounds. Since the synthesis in 1990 (*1*) of κ-phase di[bis(ethylenedithiolo)tetrathiafulvalene] copper(I)bis(isothiocyanate), $\kappa\text{-}[(ET)_2]^+[Cu(NCS)_2]^-$, which exhibits a $T_c$ = 10.4 K in dc resistance measurements, a new series of κ-phase compounds has been synthesized with $T_c$ values in excess of 11 K (*2*).

The x-ray studies of $\kappa\text{-}[(ET)_2]^+[Cu(NCS)_2]^-$ (*1*, *3*) have revealed a structure formed by the interstacking of planes of standing ET molecules that form dimers in a two-dimensional (2-D) network arrangement, together with planes formed by $[Cu(NCS)_2]$ polymer chains located between the ET planes (see Fig. 1). These structural studies have opened up discussions on the role and position of the $[Cu(NCS)_2]$ counteranions within the plane. The presence of positional disorder and a stacking fault in the direction of the *b* axis every four unit cells have been proposed (*4*). These structural models together with the idea of a diminished role in the electrical conductivity played by the anions (as insulating spacers between the ET conduction planes) have been used to explain the behavior of these κ-phase materials.

R Fainchtein, Applied Physics Laboratory, Johns Hopkins University, Laurel, MD 20723.
S. T. D'Arcangelis, S. S. Yang, D. O. Cowan, Chemistry Department, Johns Hopkins University, Baltimore, MD 21218.

*To whom correspondence should be addressed.

The electrical transport properties of the κ-phase ET compounds display a peculiar temperature behavior that is not yet fully understood. The temperature dependence of the electrical resistivity of the material reveals the existence of three regimes: (i) a metallic regime (decrease of resistance with temperature) from room temperature to 240 K; (ii) an activated or "semiconducting" regime (increase of resistance with temperature) from 240 to 90 K; and (iii) another metallic regime from 90 to 10.8 K before the compound finally makes the transition to a superconductor with a mid-range $T_c$ of 10.4 K (*5*).

In this study a scanning tunneling microscope (STM) was used in an effort to resolve the structural uncertainties and provide insight into the role of the anions in the conductivity of the material. The results may also suggest a possible explanation for the peculiar temperature dependence of the electrical resistivity in this material.

Samples of $\kappa\text{-}[(ET)_2]^+[Cu(NCS)_2]^-$ were prepared by standard electrochemical methods (*5*). Four-probe dc resistance measurements were made on single crystals from room temperature to liquid helium temperature.

STM images of $\kappa\text{-}[(ET)_2]^+[Cu(NCS)_2]^-$ were taken in air at room temperature. The measurements were made with a commercial STM (*6*) operated under either standard constant-current or constant-height conditions (*7*). No apparent differences in the images were observed in the two modes of operation. The crystals were mounted on Au films and fixed to the substrates with conductive Ag paint. The tunneling current ($i_{tun}$) was set to values of 1 nA. Scans